

A seismological study of landquakes using a real-time broad-band seismic network

Chi-Hsuan Chen,^{1,3} Wei-An Chao,¹ Yih-Min Wu,¹ Li Zhao,² Yue-Gau Chen,¹ Wan-Yun Ho,¹ Ting-Li Lin,⁴ Kuan-Hung Kuo⁵ and Jui-Ming Chang¹

¹Department of Geosciences, National Taiwan University, Taipei 10617, Taiwan. E-mail: vvnchao@gmail.com

²Institute of Earth Sciences, Academia Sinica, Taipei 11529, Taiwan

³Central Geological Survey, MOEA, Taipei 23568, Taiwan

⁴Department of Earth Sciences, National Cheng Kung University, Tainan 701, Taiwan

⁵Central Weather Bureau, Taipei 10048, Taiwan

Accepted 2013 March 25. Received 2013 March 23; in original form 2012 June 12

SUMMARY

We detected 12 landquakes in Taiwan with collapse areas between 0.27 and 2.48 km² associated with rock collapse, rockslide and debris and/or rock avalanche during the passage of Typhoon Morakot in 2009. These events were recorded by seismic stations of the Broadband Array in Taiwan for Seismology. Their locations were determined by a cross-correlation technique that maximizes the coherency of horizontal envelope function among seismic stations with a mean location error of 1.92 km. We applied time-frequency analysis to estimate the bandwidth of seismic energy generated by the landquakes. The predominant frequency ranges from 0.5 to 5.0 Hz, with higher-frequency signals likely caused by block impact. We extracted signal duration (S_D), peak ground velocity, rise time (T_R), area of velocity envelope function (A_E) from the closest station and estimated the collapse area (A_C) and run-out distance (D_R) by mapping satellite images. Based on aforementioned seismic and geometrical parameters, we defined the potential of initial impact (P_I), the frequency of rock impact signal (f_i) and the mean quasi-front velocity (V_f) as indicators of landquake types, especially for events with dam formation (dam-formation-type events). We also derived an empirical linear relationship between the envelope area (A_E) and collapse area (A_C) with a high correlation coefficient of 0.83. Our automatic approach is very effective for rapid determination of landquake centroid location and collapse area, and for identifying dam-formation event using records from existing real-time broad-band seismic networks, thus providing an important alternative for landquake hazard mitigation.

Key words: Time-series analysis; Interferometry; Geomorphology; Asia.

1 INTRODUCTION

Landslides are large rapid mass movement of the Earth surface under gravitational force, which are responsible for more than 340 fatalities each month worldwide (Petley *et al.* 2009). Thus, landslide risks have become an important issue in global natural hazard mitigation effort. Conventional seismic data analysis offers a unique approach to studying landslides that is independent of and complementary to other types of data. There are two distinct advantages provided by seismic monitoring: the abilities to detect remote events and to determine the occurrence times. Precision in occurrence time determination is helpful to analysing the temporal characteristics of landslides (e.g. rainfall-induced landslides). Landslide source mechanisms have been studied in detail for decades using long-period seismic signals (Kanamori & Given 1982; Eissler &

Kanamori 1987; Dahlen 1993; Brodsky *et al.* 2003). They concluded that the source mechanism of landslides can be represented by a nearly horizontal single forces or shallow horizontal thrust faults. They also demonstrated that landslides can generate long-period seismic signals propagating over long distances. Recently, Favreau *et al.* (2010) and Moretti *et al.* (2012) conducted numerical modelling of landslide dynamics and seismic wave generation with realistic topography to discriminate different flow scenarios and estimate the rheological parameters. They showed that the low-frequency source function (the spatio-temporal variation of the basal stress field) of a landslide is a force with horizontal and vertical components. Lin *et al.* (2010) analysed long-period (20–50 s) regional seismic records and located the landslides and submarine slumps during the Typhoon Morakot which hit Taiwan in 2009 August. Long-period signals may not be suitable for real-time

landslide monitoring and early warning purposes due to the insufficient accuracy of source location. Burtin *et al.* (2009) used the cross-correlation technique to low-frequency (0.6–0.9 Hz) signals to determine the source locations of a sequence of the Himalayan debris flow in a homogeneous velocity model with prior constraints. However, their simplified approach is best suited for a small area with a dense seismic array. In a different approach, Kao *et al.* (2012) adopted the Source-Scanning Algorithm (SSA) originally designed to locate non-volcanic tremors along subduction zones (Kao & Shan 2004; Kao *et al.* 2005). They detected five typhoon-induced large landslides using real-time high-frequency (1–8 Hz) seismic *S*-wave signals. Nevertheless, the SSA approach significantly relies on large bursts of *S*-wave energy, which are influenced by lateral heterogeneities, at multiple stations with good station coverage and sufficient signal-to-noise ratio (SNR). A poor station coverage will lead to uncertainties in both the epicentre and original time of the landslide, which have a trade-off relationship. This phenomenon has been illustrated by the discrepancy in the original time of typhoon-induced Hsiaolin landslide in 2009 in the mountain area in southern Taiwan, which claimed over 400 lives. The difference in its origin time between Kao *et al.* (2012) and Feng (2011) amounts to about 44 s.

In this study, we use the term ‘landquake’ to represent all mass-movement events such as rockfalls, rock avalanches, landslides and debris flows classified according to their dynamic behaviours. In general, landquake detection using real-time broad-band seismic signals can provide timely warnings to reduce the impending damages. Previous efforts on source characterization were mainly case studies focusing on the determination of the types of landquakes by seismogram/spectrogram analysis. Norris (1994) reviewed seismograms from 14 rockfalls and avalanches of moderate to large volumes (10^4 – 10^7 m³) at Mount St. Helens. Deparis *et al.* (2008) also presented a study on the seismic signals generated by large rockfalls and rock avalanche events in the French Alps. Vilajosana *et al.* (2008) observed sharp energetic bands over the complete frequency spectrum from the impact phase of rockfalls, which were recorded by close-by seismic stations (source–receiver distance less than 300 m). Hibert *et al.* (2011) analysed the seismic signals of hundreds of rockfall to investigate a possible link between physical rockfall-generating processes and associated seismic signal features. They found that the *P* and *S* waves cannot be distinguished due to the complexity of the source mechanism and the dominance of surface waves in the rockfall-generated seismic signal. They also showed that the fall of rocks has different characteristics than rockfall characterized by granular flow. La Rocca *et al.* (2004) analysed the seismic signals produced by two landslides that generated complex seismic signals with an irregular envelope with a frequency band between 0.1 and 5 Hz and duration of a few minutes. Suriñach *et al.* (2005) found that the spectrograms of landslides show a triangular shape due to an increase over time in the higher-frequency constituents. Feng (2011) performed time-frequency analysis by the Hilbert–Huang transform to conclude that the main frequency content of the seismic waves caused by larger landslides in the range of 0.5–1.5 Hz. Several attempts have also been made to understand the characteristics of rockslides. Weichert *et al.* (1994) proposed that rockslides signals may be distinguished from other signals by their relatively large energy content at long periods, which remain visible at stations several hundred kilometres from the event sources. Dammeier *et al.* (2011) developed quantitative estimates of fundamental rockslide properties (e.g. volume) based solely on regional seismic data. They found that the main component of the seismic energy of rockslides is

contained in frequencies below ~ 3 –4 Hz, while higher-frequency signals may be caused by block impacts. However, Hibert *et al.* (2011) showed that the seismic energy correlates well with the loss of potential energy during the mass flow over the slope. Thus, this suggests that part of the seismic energy is related to the flow rather than to the impact processes. They also proposed a method to estimate the volume of the rockfall from the generated seismic energy. Both previous studies depict similar signal characteristics including emergent onsets, slowly decaying tails and a triangular spectrogram shape.

The aforementioned studies have considered in detail the specific characteristic shapes of the calculated spectrograms associated with various types of landquakes. Based on these previous works, in our study we first focus on the landquakes occurring in the mountain area during the passage of Typhoon Morakot across Taiwan from 2009 August 7 to 10 (UTC), which resulted in 675 death, 24 missing and an estimated economic loss of \$3.3 billion (Chanson 2010). Note that, all of the times referenced in this manuscript are UTC times. We performed systematic time–frequency analysis of the real-time continuous seismic data from Broadband Array in Taiwan for Seismology (BATS) stations, in which we detected 12 large-scale landquake events and applied our location approach to determine their centroid locations. Kao *et al.* (2012) showed that the landslide-induced seismic signals exhibit a tremor-like pattern with intermittent bursts of large amplitude and lacks the distinctive arrivals of *P*- and *S*-wave phases. Thus, the location method we used is adapted from one developed for the monitoring of tremors (Wech & Creager 2008). This cross-correlation-based approach has been implemented in a near real-time system, which detects and locates tremor events on a daily basis (Wech *et al.* 2009; Wech 2010). Most of the recent studies show that the seismic phases excited by landquakes are likely composed primarily of surface (Rayleigh wave) or shear waves (Lin *et al.* 2010; Suwa *et al.* 2010; Dammeier *et al.* 2011; Feng 2011; Hibert *et al.* 2011). Our automatic location method employs a cross-correlation technique that maximizes the coherency of the horizontal envelope function in the high-frequency (1–3 Hz) waveforms at BATS stations. In order to minimize the effect of lateral heterogeneities on predicting differential *S*-wave arrival times of each station pair, we perform 3-D ray tracing (Koketsu & Sekine 1998) through the velocity model of Wu *et al.* (2007, 2009). With sufficient accuracy of source locations, we estimate the geometrical parameters (e.g. collapse area, run-out distance and slope angle) of each landquake event by the analyses of satellite images. Furthermore, we extracted signal duration, peak ground velocity (PGV), rise time, potential of initial rock impact, envelope area and the frequency of rock impact signal from each seismogram of the closest station. We also seek to establish the relationship between envelope area and the collapse area of landquakes. The empirical relationship is useful in estimating collapse area of landquake events from real-time seismic signals within a matter of minutes. Finally, we use these seismic parameters to distinguish landquake type, especially for events with dam formation (dam-formation-type events, or DFTEs). With the existing dense real-time broad-band seismic networks, our study yields an efficient automatic location approach with sufficient accuracy, robust linear relationship between envelope area and event, collapse area and effective indicators of classifying landquake event types and demonstrates a high potential in real-time landquake monitoring in Taiwan. To mitigate disasters caused by large-scale landquakes, a real-time monitoring system for rapid determinations of landquake location, type and collapse area is essential to the government emergency responses.

2 DATA PROCESSING AND ANALYSIS

2.1 Detection of landquakes

Seismic records used in this study come from stations of the BATS network, operated by the Institute of Earth Sciences of Academia Sinica and the Central Weather Bureau of Taiwan, for a wide range of seismological researches (Kao *et al.* 1998). With an average interstation distance of about 30 km, the BATS stations provide high-quality real-time continuous waveform records for routine determination of centroid moment tensor solutions. In this study, we first analyse the seismic signals caused by the Hsiaolin landquake during Typhoon Morakot in 2009. We remove from each raw record the instrument response, mean and linear trend, and then apply time-frequency analysis to examine the bandwidth of the seismic energy generated by this landquake. Fig. 1 shows the locations of the landquake and stations as well as spectrograms at selected stations. The spectrograms are calculated by the *S*-transformation (Stockwell *et al.* 1996), which takes the advantage of the well-known

theory of Fourier analysis. Similar patterns can be observed in the spectrograms at different stations, such as SGSB and YHNB are the nearest and farthest stations from the village of Hsiaolin, respectively. The discrepancy between these spectrograms is largely due to high-frequency signals generated by the landquake decaying with distance. Nevertheless, high-frequency signal is still good enough for detection by the time-frequency analysis at the farther away YHNB station. We can also see the triangular shaped spectrograms in the 1–3 Hz frequency band that are consistent with previous studies (Suriñach *et al.* 2005; Helmstetter & Garambois 2010; Dammeier *et al.* 2011; Hibert *et al.* 2011). To investigate the difference in spectrograms of different types of seismic events (local, regional/telesismic earthquakes and landquakes), we first examine the different characteristics of landquakes and local and telesismic earthquakes, as shown in Fig. 2. The spectrogram of landslide typically exhibits a triangular shape, with higher frequencies arriving later but decaying earlier. High-frequency signals between 0.5 and 5 Hz may be caused by the impact of large blocks on the ground. In

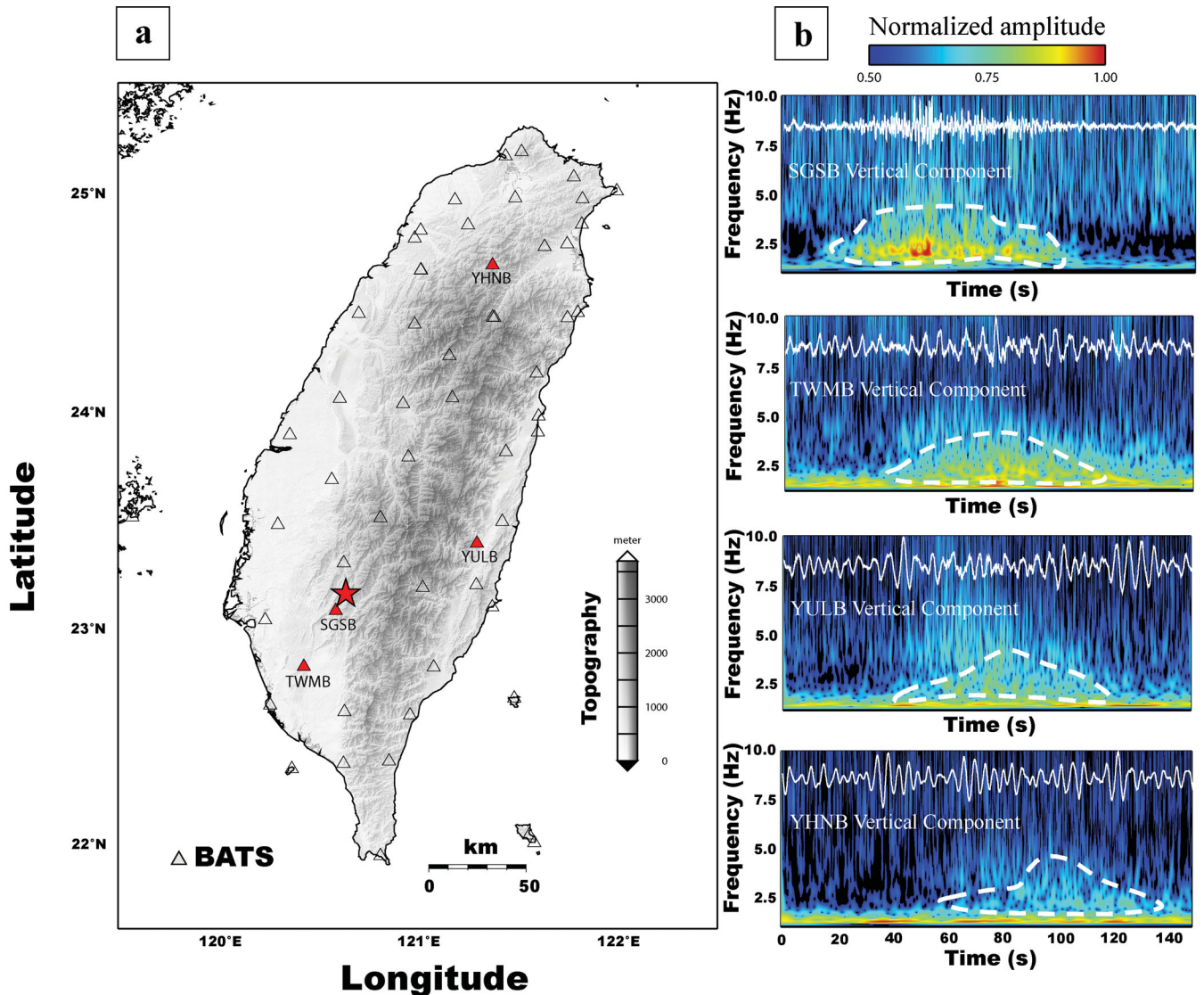


Figure 1. (a) Locations of the Shiaolin landquake (red star) and real-time seismic stations (triangles) of BATS network. Solid red triangles are stations whose spectrograms are shown in (b). (b) Vertical-component spectrograms of the Shiaolin landquake-induced ground motion. White traces are the original vertical-component velocity records. The time-frequency regions with the most energy arriving from the landquake are indicated by the white dash lines. The maximum normalized amplitude is depicted in red while the black regions indicate spectral amplitudes less than 0.5.

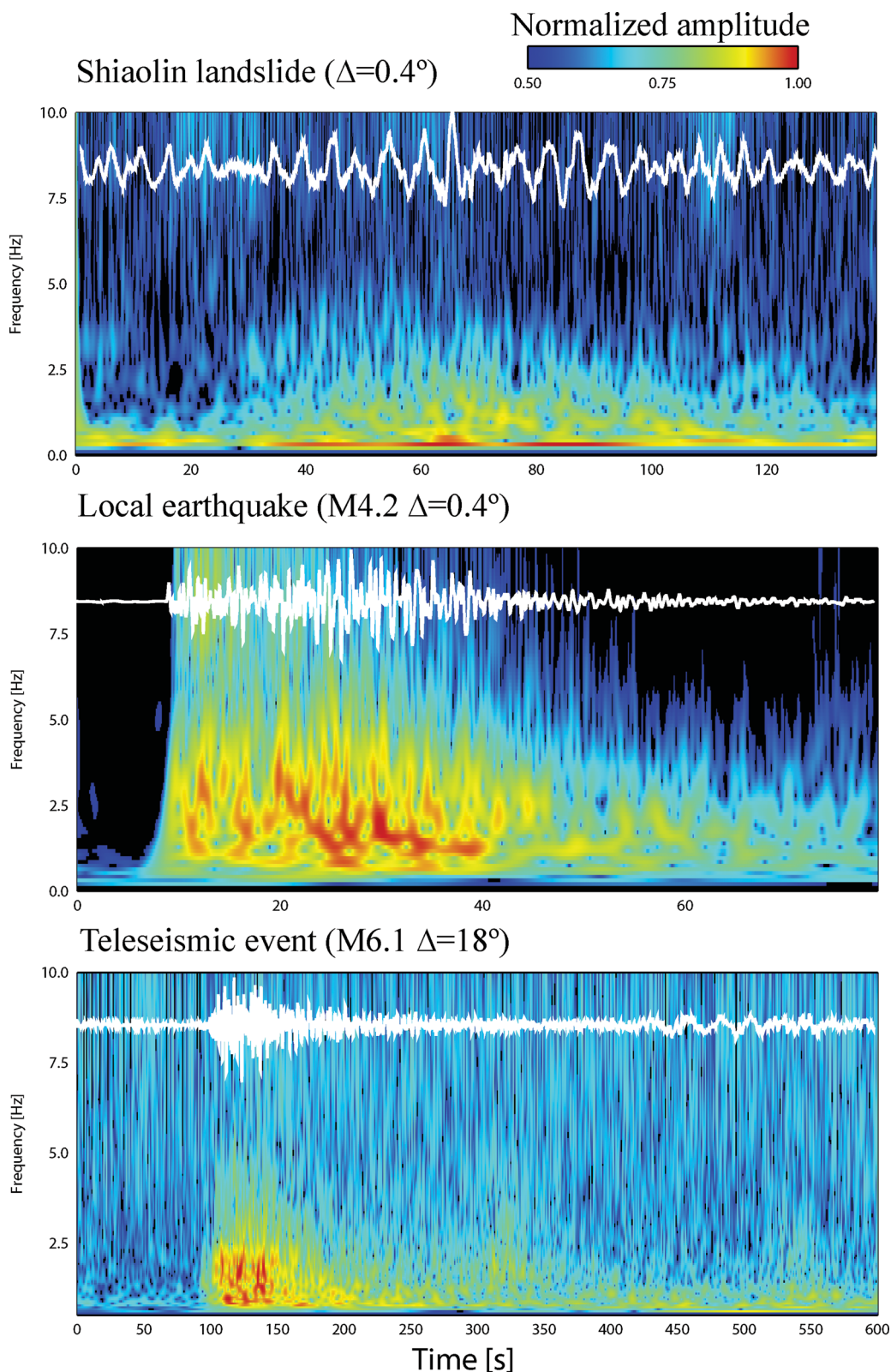


Figure 2. Comparison of the spectrograms of a landslide with local and teleseismic earthquakes. White traces are the original vertical-component velocity records. In the black regions the normalized amplitudes are less than 0.5.

contrast to landquakes, the spectrogram of local earthquake shows seismic energy of a much wider frequency content appearing suddenly after the first arrival time, followed by an exponential decay. Teleseismic event exhibits longer durations and gentler decays of

seismic energy than local earthquake. Based on these observations, we collected continuous real-time broad-band seismic data during the entire passage of Typhoon Morakot (2009 August 7–10) in Taiwan, and performed the systematic time-frequency analysis to

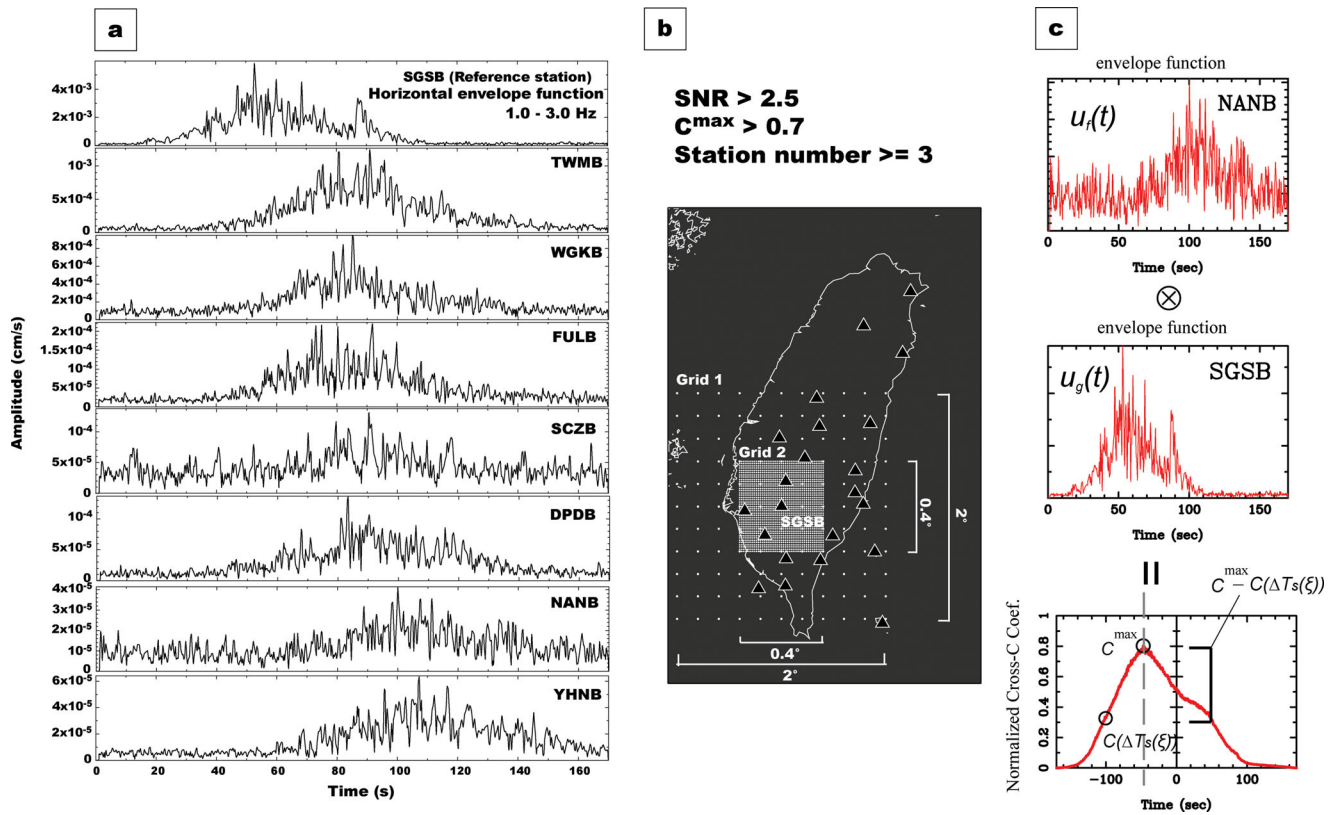


Figure 3. (a) Filtered horizontal envelope functions of ShiaoLin landquake. (b) Two stages of spatial discretization defined in the location approach. (c) An example of cross-correlation scheme between the envelope functions at stations NANB and SGSB.

detect large-scale landquakes with triangular shaped spectrograms. In the end, we detected a total of 12 large-scale landquake events and applied our location technique to determine their source centroid locations.

2.2 Location of landquakes

Unlike natural earthquakes, common seismic phases are difficult to identify in the records of landquakes. As a result, locations of landquakes can not be determined by conventional earthquake location algorithms (Hibert *et al.* 2011; Kao *et al.* 2012). In this study, we adapt a location method developed for the monitoring of tremors (Wech & Creager 2008). In our location procedure, we first collect the waveform records from BATS stations and remove the instrument response, mean and linear trend from each trace. The resulting seismograms are then bandpass filtered by a fourth-order Butterworth filter with corner frequencies of 1.0–3.0 Hz. Next, we calculate the rms amplitudes of the filtered horizontal component (E–W and N–S) waveforms to create the horizontal envelope functions for cross-correlation scheme (Fig. 3a). Complex patterns in horizontal envelope functions such as strong pulses with different frequency contents provide a good opportunity to investigate the dynamics of the mass movement using broad-band seismograms with high spatial and temporal resolutions. Favreau *et al.* (2010) and Moretti *et al.* (2012) showed that comparison of the simulated and recorded seismic waves can be used to discriminate different flow dynamics.

For scanning the landslide locations with computational efficiency, we adopt a two-stage grid search strategy. In the first stage, the seismic station with the highest SNR, which is calculated from the ratio between peak envelope amplitude and whole-term aver-

age, is selected as the centre around which a grid is established with a $\pm 1.0^\circ$ range and 0.2° spacing for both longitude and latitude (Fig. 3b). The grid point with highest cross-correlation is taken as centre to establish the second-stage finer grid with a $\pm 0.2^\circ$ range and 0.01° spacing with grid points on the free surface topography.

Previous studies have suggested that the seismic phases excited by landquakes are likely composed primarily of Rayleigh wave or shear wave (Lin *et al.* 2010; Suwa *et al.* 2010; Dammeier *et al.* 2011; Feng 2011; Hibert *et al.* 2011), and that the timing of the peak amplitude in a landquake seismogram would then be associated with the greatest mass impact on the ground (Dammeier *et al.* 2011). Nevertheless, several factors may contribute to this peak amplitude. Favreau *et al.* (2010) and Moretti *et al.* (2012) showed that the peak amplitude seems to correspond to the mass flowing down to a topography jump and coincide with a turn in the topography. Hibert *et al.* (2011) concluded that the peak amplitude builds gradually, perhaps during the granular flow over the slope. Here, we perform 3-D ray tracing (Koketsu & Sekine 1998) through the recent regional tomography model of Wu *et al.* (2007, 2009) in order to minimize the effect of lateral heterogeneities on predicting the S-wave arrival times. For a given pair of stations *f* and *g*, we calculate the cross-correlation between their horizontal envelope functions u_f and u_g . Each cross-correlogram and corresponding maximum cross-correlation coefficient (C_{fg}) are normalized by the maximum autocorrelation coefficients C_{ff} and C_{gg} of the two horizontal envelope functions:

$$C(t) = \frac{\int_{-T}^T u_f(t + \tau)u_g(\tau)d\tau}{\sqrt{C_{ff}C_{gg}}}, \quad (1)$$

Table 1. Weighting coefficient (w) used in the optimization process.

	Weighted coefficient (W)
$C^{\max} \geq 0.85$	1.0
$0.80 \leq C^{\max} < 0.85$	0.9
$0.75 \leq C^{\max} < 0.80$	0.8
$C^{\max} < 0.75$	0.7

$$C^{\max} = \frac{C_{fg}}{\sqrt{C_{ff} C_{gg}}}, \quad (2)$$

where T is the length of the time window for two target waveforms. Only events recorded by at least three seismic stations are considered in this study. Furthermore, only waveforms with normalized maximum cross-correlation coefficient (C^{\max}) and SNR ratio larger than 0.7 and 2.5, respectively, are used in our automatic location process. Fig. 3(c) displays an example of calculating the cross-correlogram and maximum cross-correlation coefficient (C_{fg}) between stations NANB and SGSB. We also define a weighting coefficient (w) in the optimization process based on the value of C^{\max} , as shown in Table 1. For a given location (ξ), we define its cross-correlation amplitude misfit A_m by the weighted sum of the vertical cross-correlation differences:

$$A_m(\xi) = \frac{1}{N_p} \sum_{i=1}^{N_p} \sum_{j=i+1}^{N_p} [C_{ij}^{\max} - C_{ij}(\Delta T_{ij}^S(\xi))] \times w_{ij}, \quad (3)$$

where ΔT^S is the theoretical differential S -wave traveltime between the two target stations from the corresponding point ξ . N_p is the number of station pairs. Generally speaking, the C^{\max} values advocate the best waveform similarity through aligning the large ampli-

tude of envelope functions at the optimal lag time. This lag time represents the difference between the observed S -wave traveltimes at the two target stations since the highest amplitude is primarily associated with shear wave. In the landquake location-scanning process, the optimal source location with the maximum coherency with respect to the ξ source point is determined by minimizing the cross-correlation amplitude misfit (A_m). The optimal location with the highest relative fitness value (R_F) is regarded as the landquake centroid location. The relative fitness is defined as:

$$R_F(\xi) = \frac{A_m^{\max} - A_m(\xi)}{A_m^{\max} - A_m^{\min}}, \quad (4)$$

where A_m^{\max} and A_m^{\min} are the maximum and minimum cross-correlation amplitude misfits, respectively. Fig. 4 shows the location result of the Shiaolin landquake during the Typhoon Morakot. The estimated centroid source of the landslide was located at (120.63°E; 23.16°N), about 1 km away from the verified location in the field (120.64°E; 23.16°N). Our location result indicates this approach is capable of determining an accurate landslide location using high-frequency signals from broad-band seismic records than previous studies (Lin *et al.* 2010; Dammeier *et al.* 2011). We have also experimented using the P -wave traveltime differences in the location process. Results show that we can not obtain accurate source centroid locations.

2.3 Estimation of location errors

To establish the correlation between the landquake centroid location and the geometrical parameters estimated from satellite image analysis, it is necessary to define the errors in our location results. For this purpose, we select 15 events from the aftershock sequence of the 2010 March 4, Jiasian earthquake in southern Taiwan.

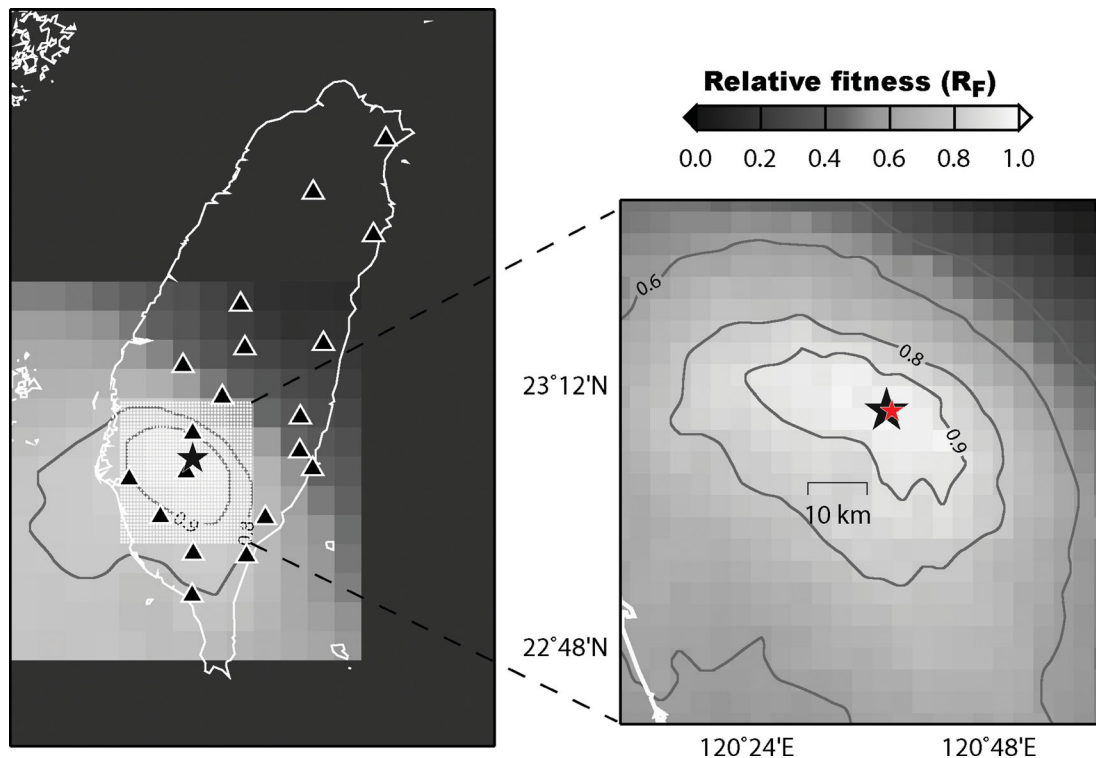


Figure 4. Left panel shows the location after the first stage and the fine grid of the second stage with grid points shown by the white dots. Solid black triangles are stations used in this location process. Black star is the location of the landquake after the second stage. Black and red stars in the right panel indicate the locations of the Shiaolin landslide from second-stage grid search and from field observation, respectively. The grey scale shows the relative fitness value R_F .

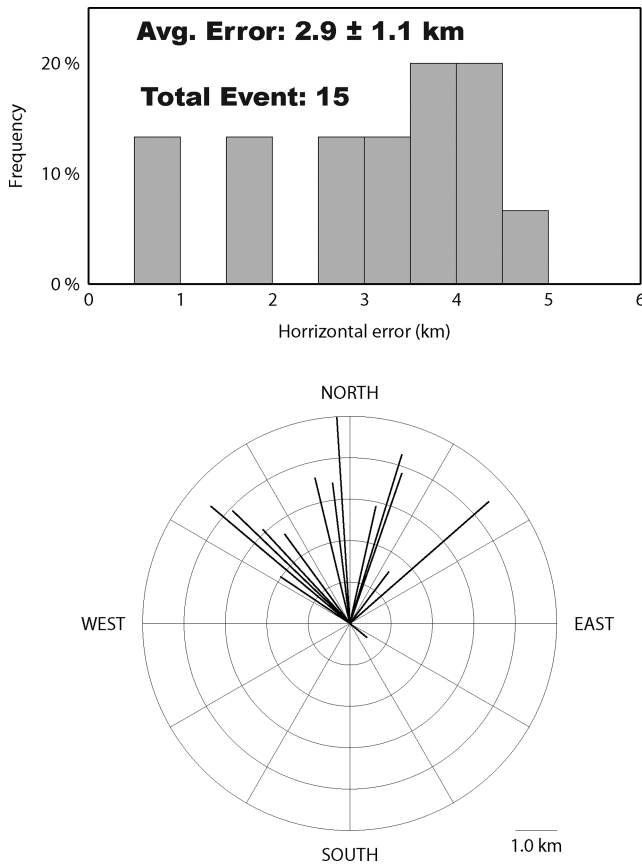


Figure 5. Distributions of the horizontal errors (top) and the azimuths (bottom) in our locations for the 15 aftershocks of the Jiasian earthquake.

These well-located aftershocks (Huang *et al.* 2011) have magnitudes M_L between 2.9 and 5.7 and are located near the typhoon-induced ShiaoLin landquake. We collected broad-band seismic records of the 15 earthquakes from BATS stations. The waveforms are processed with same procedures as in landquake analysis and the centroid locations of these earthquakes are determined from the processed records by our location approach used for the landquake. During the location process of the aftershocks, the event depths are fixed with values given in Huang *et al.* (2011). The comparison between our centroid earthquake locations and those in Huang *et al.* (2011) shows a good agreement. The error analysis is summarized in Fig. 5. For the 15 earthquakes, the horizontal errors are on average 2.9 ± 1.1 km and never exceed 5 km, and are affected by the BATS station distribution, which is relatively sparse in the mountain area, as

shown in station locations in Fig. 1 and the azimuthal distribution of the events in Fig. 5. With a similar station configuration, spatial source discretization and filtering frequency band, these well-located Jiasian aftershocks (Huang *et al.* 2011) provide a good opportunity to examine how the distribution of seismic observations can influence the determination of landquake locations. This error estimation can be used to establish the correlation between our located typhoon-induced landquakes and the possible source activity from the available satellite images.

3 RESULTS AND DISCUSSION

3.1 Landquake locations and satellite images

There landquakes were recorded by broad-band stations varying between 3 and 19 in number, with distances ranging from a minimum of 9.8 km to a maximum of 234 km. The shortest event-station distances are between 9.8 and 16.8 km. Table 2 lists the 12 landquake events with their estimated parameters and the closest BATS stations. The available satellite image data set, which consists of mapping of the landquake area by the Central Geological Survey of Taiwan before and after the Typhoon, reveals the occurrence of numerous landquake events with collapse areas larger than 0.1 km² in four representative regions, as shown in Fig. 6. Based on the mapping results, the 5-km error limit of searching radius around landquake centroid location and the seismic signal duration of events, we correlate the 12 landquake events with the mapped collapse area. As a result, the average distance between the associated landslides and our located landquakes, is 1.92 km. Event No. 1 has the largest error of 4.45 km, for which we only utilized three stations with sufficient SNR ratio to perform the location procedure. The landquake events as determined in this study can be roughly associated with active collapse areas between 0.27 and 2.48 km².

3.2 Seismic signal parameters and landquake characteristics

Recent studies have demonstrated the potential of the seismic signals in providing estimates of the geometrical properties and dynamic behavior of landquakes (La Rocca *et al.* 2004; DeParis *et al.* 2008; Vilajosana *et al.* 2008; Favreau *et al.* 2010; Dammeier *et al.* 2011; Helmstetter & Garambois 2010; Hibert *et al.* 2011; Kuo *et al.* 2011; Moretti *et al.* 2012). Therefore, one of our aims in this study is to characterize landquake events through the analysis of the broad-band seismic signals. In this respect, we first automatically detect the signal duration (S_D) in the horizontal envelope function from

Table 2. Characteristics of the 12 located typhoon-induced landquake events.

No.	T_1 -time of event (UTC)	S_D (s)	D_R (km)	V_f (m s ⁻¹)	A_C (km ²)	θ_s (°)	Long. (°E)	Lat. (°N)	Closest Sta.	Epi. Dist. (km)	Sta. Num.
1	2009/08/08 00:05:01	46	1.99	43.3	0.57	35	120.71	22.55	MASB	10.5	3
2	2009/08/08 17:05:37	87	1.44	16.6	0.83	19	120.73	22.49	MASB	16.8	4
3	2009/08/08 18:19:30	65	1.54	23.7	0.79	24	120.73	22.65	MASB	10.8	8
4	2009/08/08 20:16:18	45	1.67	37.1	0.51	26	120.75	22.57	MASB	12.9	5
5	2009/08/08 22:16:18	97	2.90	29.9	2.48	18	120.63	23.16	SGSB	9.8	19
6	2009/08/08 23:14:45	26	1.83	70.4	0.84	32	120.73	23.30	TPUB	10.2	16
7	2009/08/09 00:34:24	56	3.31	59.1	0.81	25	120.73	23.23	TPUB	13.3	11
8	2009/08/09 02:52:22	75	2.62	34.9	2.02	26	120.73	23.24	TPUB	12.7	13
9	2009/08/09 03:55:33	55	2.52	45.8	0.63	22	120.73	22.57	MASB	11.0	6
10	2009/08/09 09:31:54	83	3.03	36.5	2.27	25	120.82	22.56	ECLB	15.2	16
11	2009/08/10 03:54:39	21	1.12	53.3	0.27	33	120.77	23.24	TPUB	15.8	12
12	2009/08/10 04:22:50	72	3.35	46.5	1.20	37	120.77	23.32	TPUB	14.5	13

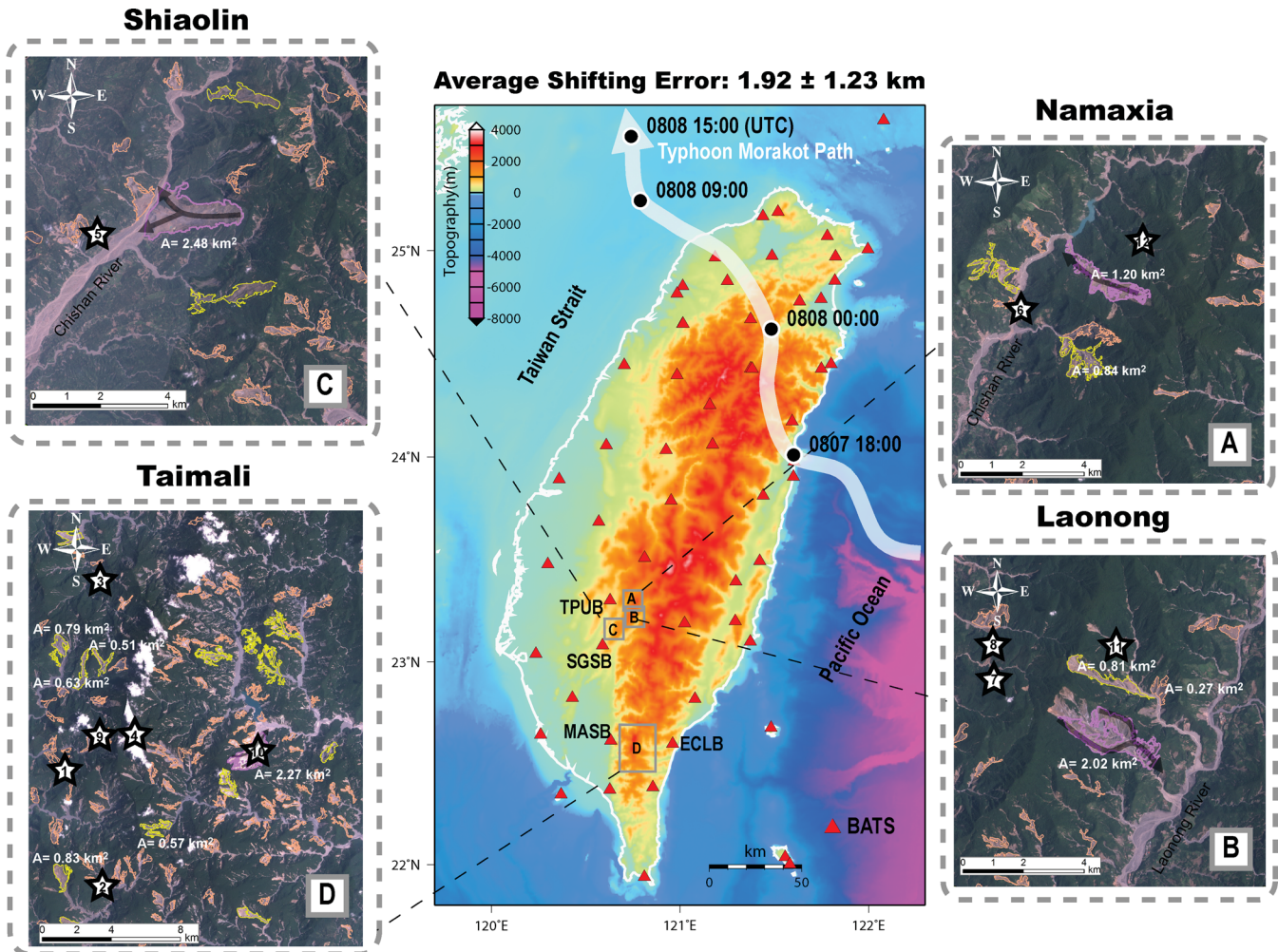


Figure 6. Middle panel: Taiwan map showing the BATS seismic stations (red triangles). The thick white line with an arrow depicts the path of Typhoon Morakot during 2009 August 7–8. Panels (a)–(d): Open stars numbered 1–12 indicate the epicentres of typhoon-induced landslide events determined in this study. These events are located in four towns. They are Namaxia (a), Laonong (b), Shiaolin (c) and Taimali (d). The arrows indicate the main run-out paths of four large-scale landslide events with dam formation (DFTEs). Areas marked by purple, yellow and orange colours indicate landslides with collapse areas larger than 1.0, 0.5 and 0.1 km², respectively, as mapped by the Central Geological Survey of Taiwan.

the closest seismic station based on a short-term average/long-term average (STA/LTA) approach widely used for real-time first-motion detections in seismology. The detection algorithm used in this study employs the ratio between the averages in 0.5 s short and 10 s long time windows in the horizontal envelope functions. An example is shown in Fig. 7(a), STA/LTA ratio threshold of 3 is adopted in this study for determining the onset time T_1 of a landslide event. Following T_1 , the PGV is also estimated from the horizontal envelope function, and the stopping time T_2 is reached of when the amplitude of the horizontal envelope function drops below 5 per cent of the PGV amplitude for at least 5 s. The time between T_1 and T_2 is defined as the duration S_D of the landslide. For seismic records with higher noise level (SNR < 6.0), we use a level of 20 per cent of the PGV amplitude in determining the stopping time T_2 (Fig. 7). After finding the corresponding signal duration S_D of the landslide event, we extract the rise time T_R , the potential of initial impact P_1 , the area of envelope function A_E and the frequency of the rock impact signal f_1 from the closest seismic record of each landslide event. Dammeier *et al.* (2011) suggested that the PGV amplitude in a landslide seismogram may be associated with the time of the greatest mass impact on the slope, whereas the envelope area A_E

may correspond to the total energy release of landslide event, with the integral relation:

$$A_E = \int_{T_1}^{T_2} (E(t) - E_0) dt. \quad (5)$$

Here E is the rms amplitudes of the filtered horizontal-component waveforms, and T_1 and T_2 are previously defined as onset and stopping times, respectively. We note here that A_E is the envelope area relative to the ambient noise level (E_0), and E_0 is defined as $(A_1 + A_2)/2$. The values of A_1 and A_2 are envelope amplitudes at time points T_1 and T_2 , respectively. In order to classify the different landslide types, we introduce three new parameters: the potential of initial impact P_1 , frequency of rock impact signal f_1 and mean quasi-front velocity V_f :

$$P_1 (\%) = (1 - T_R/S_D) \times 100\%, \quad (6)$$

$$f_1 (\text{Hz}) = \text{PGV}/A_E, \quad (7)$$

$$V_f (\text{m s}^{-1}) = D_R/S_D. \quad (8)$$

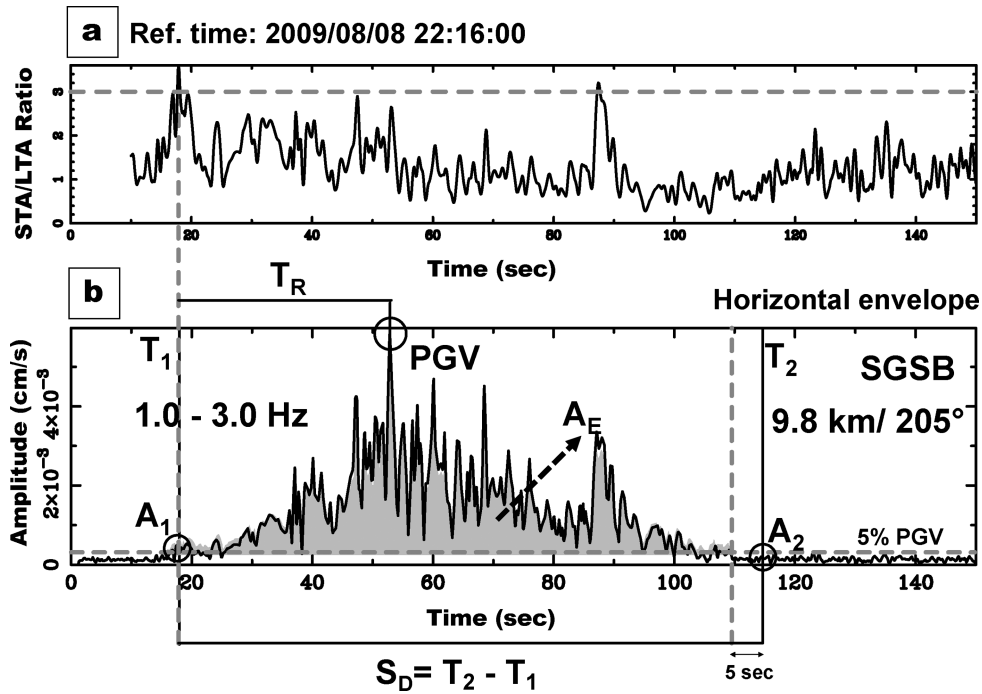


Figure 7. Example showing the determinations of seismic parameters: signal duration S_D , rise time T_R and envelope area A_E from the closest seismic record of the Shiaolin landquake.

Here T_R is the rise time and D_R is the run-out distance. Fig. 7(b) displays an example of determining these parameters from the closest station SGSB for the Shiaolin landquake event. In general, landquake events are categorized according to the type of mass movement (e.g. fall, slide and flow). The front velocity of different types varies wildly. In the case of rockfall, the materials move rapidly and almost vertically. We expect a small T_R and a high P_1 , corresponding to a single-largest rock impact with a point-source signature with a high f_1 value. In contrast, the front velocity of a debris flow ranges from 6 to 10 $m s^{-1}$ (Takahashi 2010), which is a relative slow mass movement. For an avalanche-type event, the front velocity has a broad range from 20 to 50 $m s^{-1}$ (Kuo *et al.* 2011; Tsou *et al.* 2011). Therefore, the behaviour of an avalanche event exhibits a longer T_R and a smaller P_1 than rockfall, and its seismic signal is the superposition of multipoint sources with a lower f_1 value, corresponding to individual blocks impacting and rolling along a long run-out slope. However, the behaviour of landquakes is also influenced by the other factors such as geometrical, material and frictional properties and topography effects, leading to a large variability in front velocities (Legros 2002; Sosio *et al.* 2008; Favreau *et al.* 2010; Moretti *et al.* 2012).

We first establish a linear relationship between the envelope area A_E and collapse area A_C . For regression analysis, each envelope area A_E is normalized by a value of A_0 , which is the envelope area corresponding to event No. 11 with smallest collapse area. The fitting of regression, as shown in Fig. 8(a), is good with a linear correlation coefficient of 0.83. In order to evaluate the capability of the BATS network in detecting landquakes, we also carry out a distance dependency analysis by selecting the farthest seismic stations at which the 12 landquakes are detected. The result in Fig. 8(b) shows a clear trend with the detectable source-station distance decreasing with the envelope area A_E , or the total energy release. Naturally, the limit of detection also depends on the SNR ratio as well as the type of landquakes.

The duration of a landquake event may vary widely with the size, shape and complexity of its source where some portions may have already stopped while mass movement in other portions continues, generating a long signal with gradually decreasing amplitude. Signal duration is thus comparable to the event duration (Norris 1994; McSaveney 2002; Favreau *et al.* 2010; Hibert *et al.* 2011; Moretti *et al.* 2012). In the Shiaolin landquake event (No. 5 in Table 2), our estimations of the signal duration S_D at the closest station and the mean quasi-front velocity V_f are 97 s and 29.9 $m s^{-1}$, respectively. These values are comparable to the dynamic modelling of Kuo *et al.* (2011), which concluded that the overall duration of the Shiaolin landslide was about 110 s with the maximum speed reaching 40–50 $m s^{-1}$. Our results are consistent with the study of the Thurwieser landslide, which has been recorded on video. Favreau *et al.* (2010) showed similar values of the source duration (75–90 s), the run-out distance (2900 m), the maximum front velocity ($\sim 60 m s^{-1}$) and the mean quasi-front velocity ($\sim 35 m s^{-1}$). Fig. 9 shows the waveforms and spectrograms of two events at the closest stations. The maximum normalized amplitudes are depicted in red while the black regions indicate spectral amplitudes less than 0.5. Spectrogram of the Shiaolin event (No. 5) shows a well-defined triangular shape with a primary frequency range of 0.5–5 Hz. The highest spectral amplitude occurs at ~ 50 s with frequencies of 1–2 Hz, which may correspond to the greatest block impacting the ground slope. This is also similar to the Thurwieser landslide (Favreau *et al.* 2010), even though the detailed behaviour of a landquake is influenced by multiple factors involving geometrical and material properties of the source area. The horizontal envelope function also exhibits large amplitude with a relative long-period signal at a later time of ~ 85 s. According to the dynamic modelling of Kuo *et al.* (2011), this signal might be related to the mass sliding into the Chishan River, blocking the river and creating a large lake. In Fig. 9(b) for event No. 10, we can also observe the similar long-period signals at ~ 128 s that may come from mass sliding into the Taimali River and

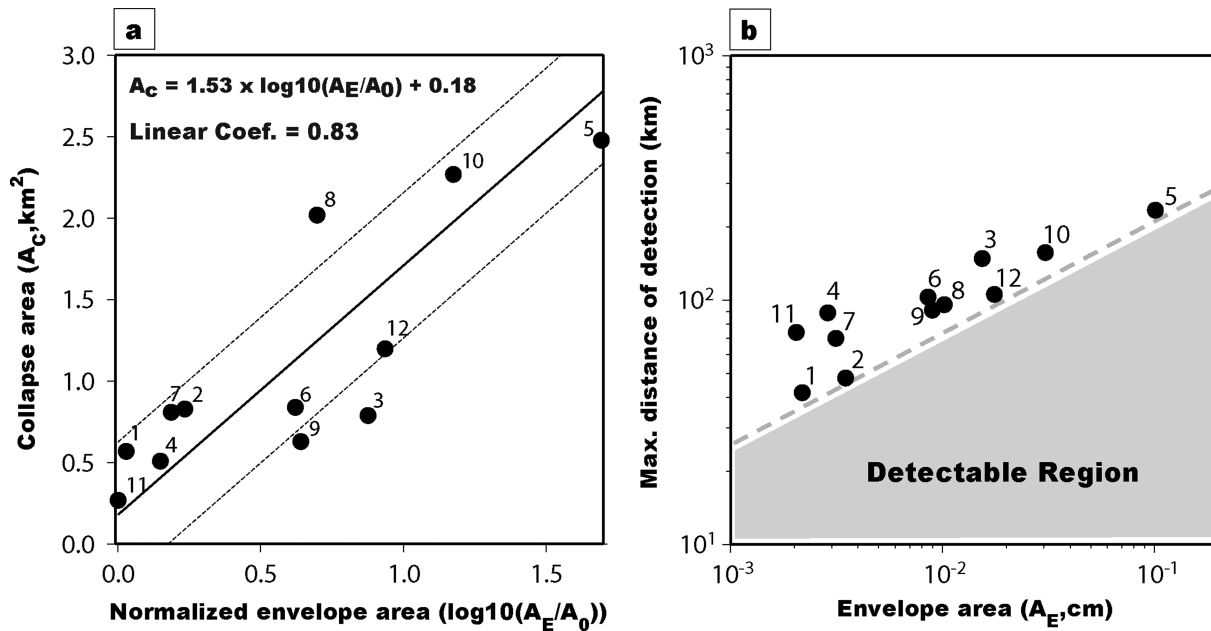


Figure 8. (a) Regression for the relationship between the logarithmic envelope area A_E relative to A_0 and the collapse area A_C . Solid line shows the regression line and the two dashed lines indicate the range of one standard deviation. The numbered dots indicate the landquake event IDs in Table 2. (b) Maximum distance of event detection as a function of envelope area A_E . Grey area below the dashed line delineates the detectable region.

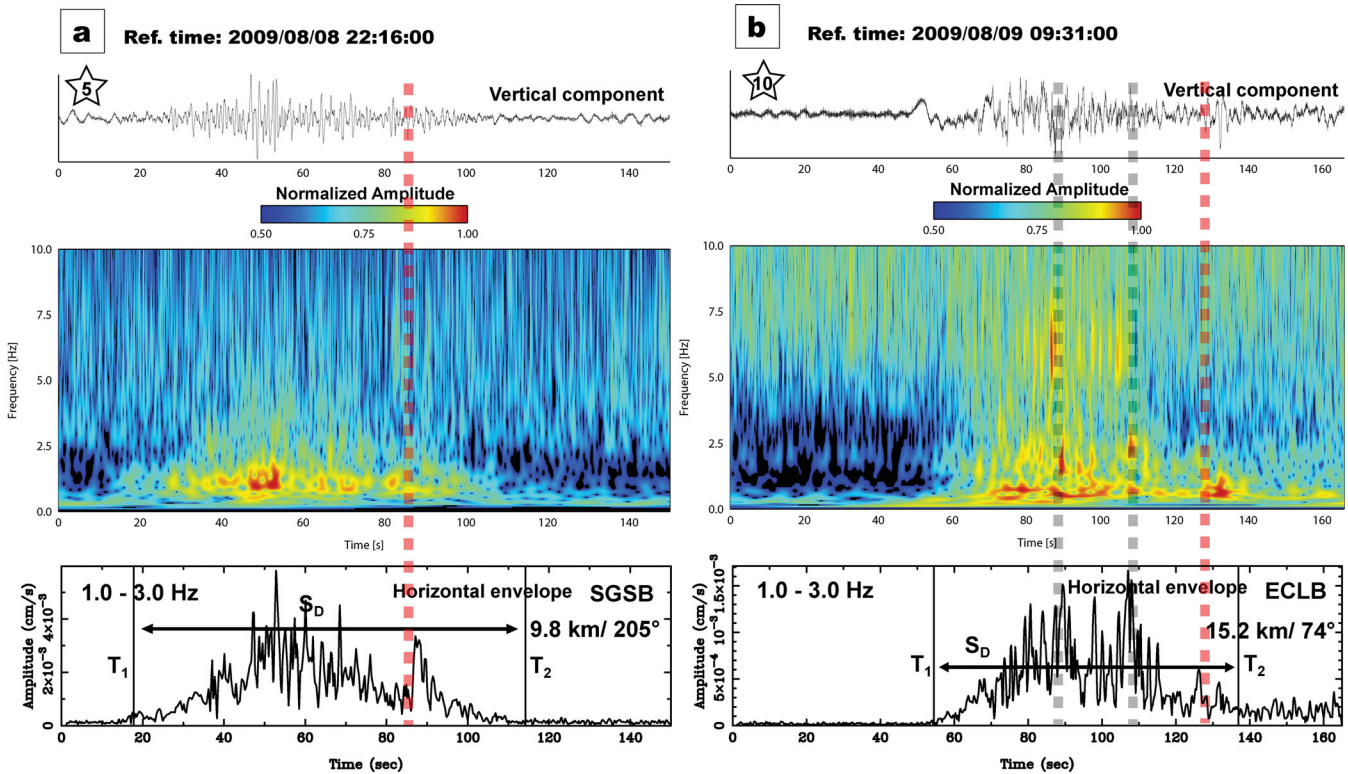


Figure 9. (a) Vertical-component seismogram (top) and spectrogram (middle) and the filtered horizontal envelope function (bottom) of event No. 5 in Table 2 at the closest station SGSB. The thick red dashed line indicates the wave packet generated by mass sliding into the river. The frequency band, epicentral distance and station azimuth are given in the bottom panel. (b) Same as (a) but for event No. 10 in Table 2 at the closest station ECLB. The thick grey and red dashed lines indicate energetic high-frequency pulses and wave packet generated by mass sliding into the river, respectively.

also forming a dam in Taimali River Valley. Helmstetter & Garambois (2010) concluded that the differences in the shaped spectrogram might be explained by the frequency- and distance-dependent attenuation and/or the material properties. Here the shortest event-station distances of the 12 landquake events are similar (between

9.8 and 16.8 km). Thus, the spectrogram of event No. 10 exhibits long-period seismic energy, with several energetic high-frequency (>5 Hz) pulses, which may be interpreted as rock sliding against the slate material on the ground in the Taimali region. The long-period signals and high-frequency pulses were excited by mechanisms of

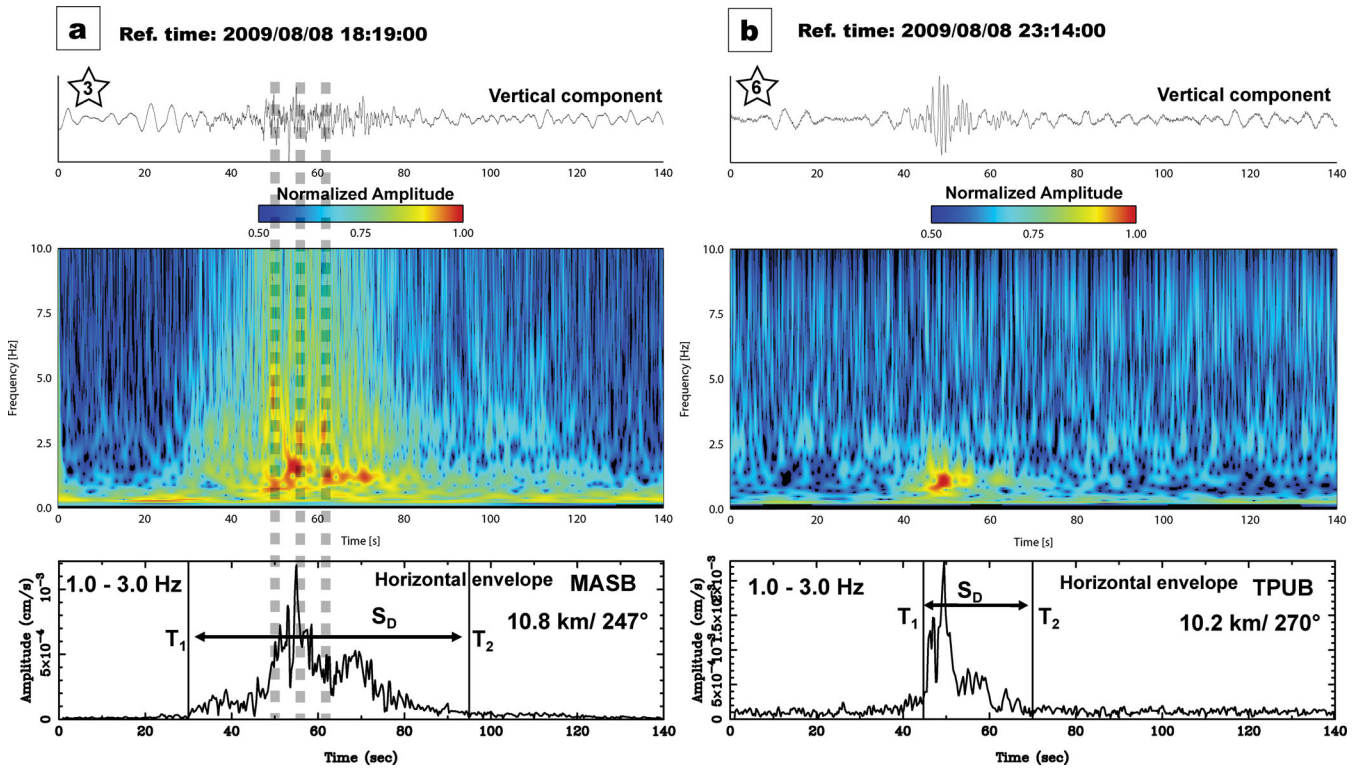


Figure 10. (a) Vertical-component seismogram (top) and spectrogram (middle) and the filtered horizontal envelope function (bottom) of event No. 3 at the closest station MASB. The thick grey dashed lines indicate the energetic high-frequency pulses. The frequency band, epicentral distance and station azimuth are given in the bottom panel. (b) Same as (a) but for event No. 6 at the closest station TPUB.

mass sliding along the cleavage plane and large block impacting and/or rolling on the failure slope, respectively. The relatively small events of Nos. 1, 3, 4 and 9 that occurred in the Taimali region also show similar high-frequency pulses with short signal durations ($45 < S_D < 65$) in their spectrograms. The only exception is event No. 2, which shows a smaller P_1 and lower f_i due to its relative longer signal duration S_D that may be caused by the fracturing of the mass due to large block impact and/or slide after rolling on a gentle slope with low slope angle (θ_s). In general, the type of rapid mass movement corresponds to rock collapses. We expect events Nos. 6, 7 and 11 are rock collapses with the mass falling and/or bouncing at very rapid speeds ($V_f > 50 \text{ m s}^{-1}$). Fig. 10 displays the waveforms and spectrograms of events of No. 3 and 6, respectively. In this study, one of our aims is to extract relevant information of landquake characteristics from seismic records, which can help identify the landquake events, especially the large-scale ones with dam formation (DFTEs). The large-scale events in this study (Nos. 5, 8, 10 and 12) all occurred in the mountain area with dam formation based on field observations, eyewitness and local news. They also generated complex seismic signals with irregular horizontal envelope functions, in a frequency band of 0.5 and 5 Hz and durations of a few minutes. These DFTEs have relatively large envelope area ($A_E > 0.01$) and low P_1 and f_i values, and their mean quasi-front velocities V_f range from 29.9 to 46.5 m s^{-1} . The relative high f_i value of No. 12 DFTE may associate with higher slope angle θ_s and/or larger mean quasi-front velocity V_f . The wider range of front velocity, longer S_D and higher A_E correspond to an avalanche-type behaviour with large amount of material moving down a long run-out slope under gravity and inducing ground vibrations. Fig. 11 summarizes the aforementioned classification of landquake characteristics. We highlight the landquake events with the above characteristics, which have a high

potential to become a DFTE. It is essential to the early warning purpose for dam-breaking flood hazards, which pose serious threats to residents downstream.

3.3 Characteristics of PGV caused by landquake

The relationship between the peak amplitude of seismic waves and the distance from the hypocentre or epicentre can be empirically established for earthquake hazard assessment purpose. Here, we investigate the variation of the PGV in the horizontal envelope function as a function of the epicentral distance to the closest station. Fig. 12 shows the PGV distance relationship for the 12 landquake events detected in this study. We observe two distinct PGV distance attenuation relations. The attenuation of small-scale events with collapse areas A_C less than 1 km^2 follow the lower curve. However, for the large-scale landquake events Nos. 5, 8, 10 and 12 with collapse areas (A_C) larger than 1 km^2 , their PGV do not decay along the same attenuation curve. They exhibit the directivity effect of mass movement at the source. For example, the anomalously high PGV of event No. 12 ($A_C = 1.2 \text{ km}^2$) occurs at station TPUB with the azimuth of 261° , almost the same as the direction of the mass movement. On the contrary, the PGV of event No. 8 ($A_C = 2.02 \text{ km}^2$) shows a relatively small value at the same station with an azimuth of 302° , in the reverse direction of the mass movement. Apart from the source directivity effect, the PGV is also affected by the propagation and/or site effects. Event No. 1 has an anomalous attenuation behaviour, which may be attributable to its large location error of 4.45 km since only three stations with sufficient SNR ratio are used in its location process.

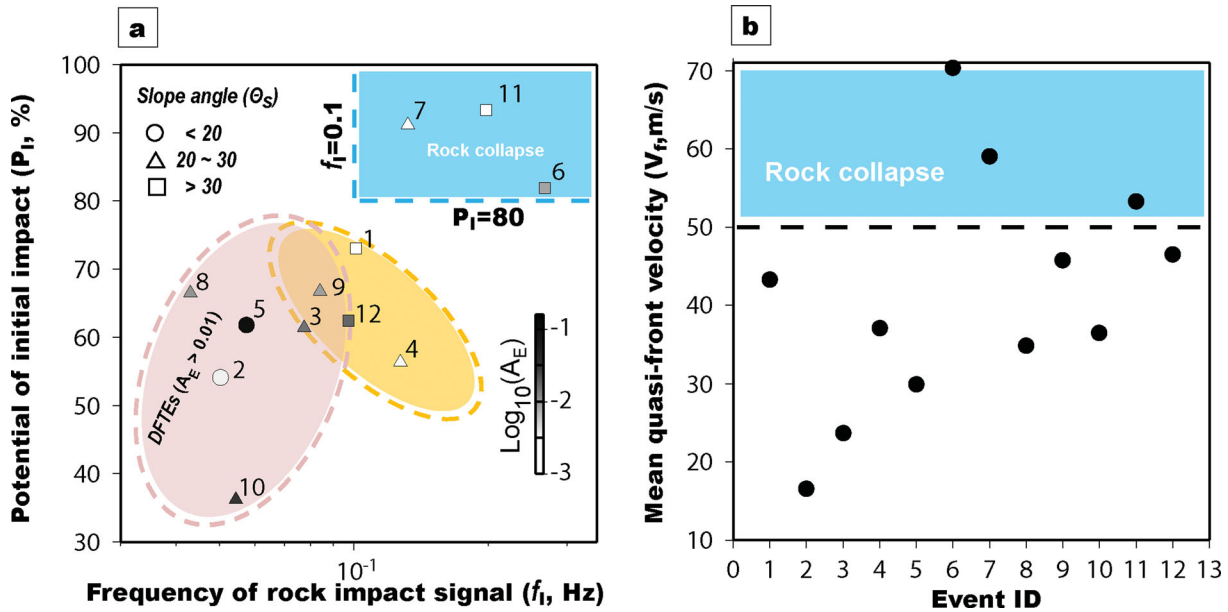


Figure 11. (a) Classification of the types of the 12 landquake events (numbered symbols) located in this study based on their f_i and P_i values. Different symbols correspond to different average slope angles θ_s . Grey scale indicates the envelope area A_E . The dashed line delineates regions of different event types. (b) Distribution of the mean quasi-front velocity V_f for the 12 landquake events.

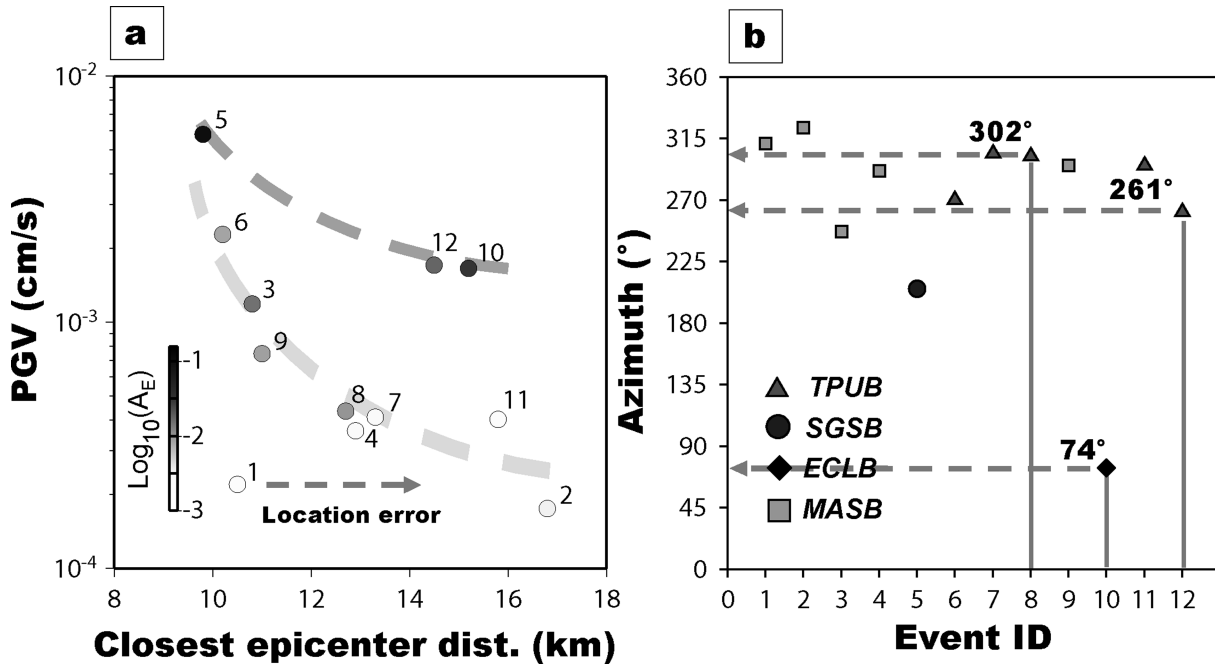


Figure 12. (a) Relationship between the epicentral distance of the closest station and peak ground velocity (PGV) of the horizontal envelope function. Grey scale indicates the envelope area A_E . Two probable PGV distance attenuation relationships are indicated by the two dashed curves. (b) Distribution of the azimuth of source-station for the 12 landquake events. Different symbols indicate different seismic stations closest to a specific event.

4 CONCLUSIONS

With the aim of studying landquake characteristics and their relations to the geometrical parameters, we analysed landquake-induced seismic signals during the 2009 Typhoon Morakot using real-time broad-band seismic waveform records. We detected a total of 12 landquake events with collapse area (A_C) between 0.27 and 2.48 km². However, Burtin *et al.* (2008) pointed out that the high level of high-frequency energy can be attributed to the turbulence of the streams in conjunction with the ground vibra-

tions generated by the transportation of sediments. The resulting increase of high-frequency seismic noise from the sediment transportation may overwhelm the landquake-induced seismic signals and limit the detection capability of the current BATS seismic networks. In order to improve the ability of detection, especially of relatively small landquake events, deployment of more broad-band seismic stations is needed. It is helpful for studying rainfall-induced landquake events and further establishing the rainfall threshold for the purpose of onsite landquake warning (Gabet *et al.* 2004).

We also established a linear relationship between the collapse area A_C and the envelope area A_E using the 12 detected landquake events with a high linear correlation coefficient of 0.83. This allows for a rapid determination of the collapse area after landquakes using real-time broad-band seismic records, and provides important and useful information for landquake hazard evaluation. Our findings also affirm the feasibility and validity of using seismic signals for the detection of landquake events (time-frequency distribution in spectrogram), determination of landquake centroid locations by cross-correlation and the classification of event type based on a few seismic parameters (e.g. PGV, S_D and A_E) and the mean quasi-front velocity V_f . In particular, the DFTEs can be quickly identified by an A_E value larger than 0.01, relatively low P_f and f_f values and a V_f range of 30–47 m s⁻¹, which can be estimated from the horizontal envelope function (E) at the closest station. Consequently, our approach developed in this study is useful in detecting, locating and characterizing landquake events, and offers a high potential for a real-time landquake-monitoring system using pre-existing seismic networks.

ACKNOWLEDGEMENTS

The authors wish to thank an anonymous reviewer for their constructive comments that helped improve the manuscript. This research has been supported by the Central Weather Bureau and the National Science Council of the Republic of China. The authors acknowledge the Central Weather Bureau and Academia Sinica, Taiwan for providing the broad-band seismic data. The collapse areas of the landquake events were provided by Central Geological Survey (CGS). The figures were created using the Generic Mapping Tools (GMT) of Wessel & Smith (1991).

REFERENCES

- Brodsky, E.E., Gordeev, E. & Kanamori, H., 2003. Landslide basal friction as measured by seismic waves, *Geophys. Res. Lett.*, **30**(24), 2236, doi:10.1029/2003GL018485.
- Burtin, A., Bollinger, L., Vergne, J. & Nábělek, J.L., 2008. Spectral analysis of seismic noise induced by rivers: a new tool to monitor spatiotemporal changes in stream hydrodynamics, *J. geophys. Res.*, **113**, B05301, doi:10.1029/2007JB005034.
- Burtin, A., Bollinger, L., Cattin, R., Vergne, J. & Nábělek, J.L., 2009. Spatiotemporal sequence of Himalayan debris flow from analysis of high-frequency seismic noise, *J. geophys. Res.*, **114**, F04009, doi:10.1029/2008JF001198.
- Chanson, H., 2010. The impact of Typhoon Morakot on the southern Taiwan coast, *Shore Beach*, **78**(2), 33–37.
- Dahlen, F.A., 1993. Single-force representation of shallow landslide sources, *Bull. seism. Soc. Am.*, **83**(1), 130–143.
- Dammeier, F., Moore, J.R., Haslinger, F. & Loew, S., 2011. Characterization of Alpine rockslides using statistical analysis of seismic signals, *J. geophys. Res.*, **116**, F04024, doi:10.1029/2011JF002037.
- Deparis, J., Jongmans, D., Cotton, F., Baillet, L., Thouvenot, F. & Hantz, D., 2008. Analysis of rock-fall and rock-fall avalanche seismograms in the French Alps, *Bull. seism. Soc. Am.*, **98**, 1781–1796.
- Eissler, H.K. & Kanamori, H., 1987. A single-force model for the 1975 Kalapana, Hawaii, earthquake, *J. geophys. Res.*, **92**, 4827–4836.
- Favreau, P., Mangeny, A., Lucas, A., Crosta, G. & Bouchut, F., 2010. Numerical modeling of landquakes, *Geophys. Res. Lett.*, **37**, L15305, doi:10.1029/2010GL043512.
- Feng, Z., 2011. The seismic signatures of the 2009 Shiaolin landslide in Taiwan, *Nat. Hazards Earth Syst. Sci.*, **11**, 1559–1569.
- Gabet, E.J., Burbank, D.W., Putkonen, J.K., Pratt, B.A.-S. & Ojha, T., 2004. Rainfall thresholds for landsliding in the Himalayas of Nepal, *Geomorphology*, **63**, 131–143.
- Helmstetter, A. & Garambois, S., 2010. Seismic monitoring of Sèchilienne Rockslide (French Alps): analysis of seismic signals and their correlation with rainfalls, *J. geophys. Res.*, **115**, F03016, doi:10.1029/2009JF001532.
- Hibert, C., Mangeny, A., Grandjean, G. & Shapiro, N.M., 2011. Slope instabilities in Dolomieu crater, Réunion Island: from seismic signals to rockfall characteristics, *J. geophys. Res.*, **116**, F04032, doi:10.1029/2011JF002038.
- Huang, H.H., Wu, Y.M., Lin, T.L., Chao, W.A., Shyu, J.B.H., Chan, C.H. & Chang, C.H., 2011. The preliminary study of the 4 March 2010 M_w 6.3 Jiasian, Taiwan, earthquake sequence, *Terr. Atmos. Ocean. Sci.*, **22**, 283–290.
- Kanamori, H. & Given, J.W., 1982. Analysis of long-period seismic waves excited by the May 18, 1980, eruption of Mount St. Helens: a terrestrial monopole? *J. geophys. Res.*, **87**, 5422–5432.
- Kao, H. & Shan, S.J., 2004. The source-scanning algorithm: mapping the distribution of seismic sources in time and space, *Geophys. J. Int.*, **157**, 589–594.
- Kao, H., Jian, P.R., Ma, K.F., Huang, B.S. & Liu, C.C., 1998. Moment-tensor inversion for offshore earthquakes east of Taiwan and their implications to regional collision, *Geophys. Res. Lett.*, **25**, 3619–3622.
- Kao, H., Shan, S.J., Dragert, H., Rogers, G., Cassidy, J.F. & Ramachandran, K., 2005. A wide depth distribution of seismic tremors along the northern Cascadia margin, *Nature*, **436**, 841–844.
- Kao, H. *et al.*, 2012. Locating, monitoring, and characterizing typhoon-induced landslides with real-time seismic signals, *Landslides*, **9**, 557–563.
- Koketsu, K. & Sekine, S., 1998. Pseudo-bending method for three-dimensional seismic ray tracing in a spherical earth with discontinuities, *Geophys. J. Int.*, **132**(2), 339–346.
- Kuo, C.Y. *et al.*, 2011. The landslide stage of the Hsiaolin catastrophe: simulation and validation, *J. geophys. Res.*, **116**, F04007, doi:10.1029/2010JF001921.
- La Rocca, M., Galluzzo, D., Saccorotti, G., Tinti, S., Cimini, G.B. & Del Pezzo, E., 2004. Seismic signals associated with landslides and with a tsunami at Stromboli Volcano, Italy, *Bull. seism. Soc. Am.*, **94**, 1850–1867.
- Legros, F., 2002. The mobility of long-runout landslides, *Eng. Geol.*, **63**, 301–331.
- Lin, C.H., Kumagai, H., Ando, M. & Shin, T.C., 2010. Detection of landslides and submarine slumps using broadband seismic networks, *Geophys. Res. Lett.*, **37**, L22309, doi:10.1029/2010GL044685.
- McSaveney, M.J., 2002. Recent rockfalls and rock avalanches in Mount Cook National Park, New Zealand, *Rev. Eng. Geol.*, **15**, 35–70.
- Moretti, L., Mangeny, A., Capdeville, Y., Stutzmann, E., Huggel, C., Schneider, D. & Bouchut, F., 2012. Numerical modeling of the Mount Steller landslide flow history and of the generated long period seismic waves, *Geophys. Res. Lett.*, **39**, L16402, doi:10.1029/2012GL052511.
- Norris, R.D., 1994. Seismicity of rockfalls and avalanches at 3 Cascade Range volcanoes: implications for seismic detection of hazardous mass movement, *Bull. seism. Soc. Am.*, **84**(6), 1925–1939.
- Petley, D.N., Rosser, N. & Parker, R., 2009. Quantifying the impacts of landslides on society, *EOS, Trans. Am. geophys. Un.*, **90**(52, Fall Meet. Suppl.), Abstract NH52A-04.
- Sosio, R., Crosta, G.B. & Hungr, O., 2008. Complete dynamic modeling calibration for the Thurwieser rock avalanche (Italian Central Alps), *Eng. Geol.*, **100**(1–2), 11–26.
- Stockwell, R.G., Mansinha, L. & Lowe, R.P., 1996. Localization of the complex spectrum: the S transform, *IEEE Trans. Signal Process.*, **44**(4), 998–1001.
- Suriñach, E., Vilajosana, I., Khazaradze, G., Biescas, B., Furdada, G. & Vilaplana, J.M., 2005. Seismic detection and characterization of landslides and other mass movements, *Nat. Hazards Earth Syst. Sci.*, **5**, 791–798.
- Suwa, H., Mizuno, T. & Ishii, T., 2010. Prediction of a landslide and analysis of slide motion with reference to the 2004 Ohto slide in Nara, Japan, *Geomorphology*, **124**(3–4), 157–163.
- Takahashi, T., 2010. *Debris Flow: Mechanics, Prediction and Countermeasures*, Taylor and Francis, London, 448 pp.

- Tsou, C.Y., Feng, Z.Y. & Chigira, M., 2011. Catastrophic landslide induced by Typhoon Morakot, Shiaolin, Taiwan, *Geomorphology*, **127**, 166–178.
- Vilajosana, I., Suriñach, E., Abellán, A., Khazaradze, G., Garcia, D. & Llosa, J., 2008. Rockfall induced seismic signals: case study in Montserrat, Catalonia, *Nat. Hazards Earth Syst. Sci.*, **8**, 805–812.
- Wech, A.G., 2010. Interactive tremor monitoring, *Seism. Res. Lett.*, **81**, 664–669.
- Wech, A.G. & Creager, K.C., 2008. Automated detection and location of Cascadia tremor, *Geophys. Res. Lett.*, **35**, L20302, doi:10.1029/2008GL035458.
- Wech, A.G., Creager, K.C. & Melbourne, I., 2009. Seismic and geodetic constraints on Cascadia slow slip, *J. geophys. Res.*, **114**, B10316, doi:10.1029/2008JB006090.
- Weichert, D., Horner, R.B. & Evans, S.G., 1994. Seismic signatures of landslides—the 1990 Brenda Mine collapse and the 1965 Hope rock-slides, *Bull. seism. Soc. Am.*, **84**(5), 1523–1532.
- Wessel, P. & Smith, W., 1991. Free software helps map and display data, *EOS, Trans. Am. geophys. Un.*, **72**(41), 441–446.
- Wu, Y.M., Chang, C.H., Zhao, L., Shyu, J.B.H., Chen, Y.G., Sieh, K. & Avouac, J.P., 2007. Seismic tomography of Taiwan: improved constraints from a dense network of strong-motion stations, *J. geophys. Res.*, **112**, B08312, doi:10.1029/2007JB004983.
- Wu, Y.M., Shyu, J.B.H., Chang, C.H., Zhao, L., Nakamura, M. & Hsu, S.K., 2009. Improved seismic tomography offshore northeastern Taiwan: implications for subduction and collision processes between Taiwan and the southernmost Ryukyu, *Geophys. J. Int.*, **178**, 1042–1054.